Charge Transport in C$_{60}$-Based Dumbbell-type Molecules: Mechanically Induced Switching between Two Distinct Conductance States

Pavel Moreno-García,*,[†] Andrea La Rosa,*,[‡,†] Viliam Kolivoška,*,[†,§] Daniel Bermejo,[‡] Wenjing Hong,[†] Koji Yoshida,[†] Masoud Baghernejad,[†] Salvatore Filippone,[‡] Peter Broekmann,[†] Thomas Wandlowski,[†] and Nazario Martín*,[‡,∥]

[†]Department of Chemistry and Biochemistry, University of Bern, Freiestrasse 3, CH-3012 Bern, Switzerland

[‡]Departamento de Química Orgánica, Facultad de Química, Universidad Complutense de Madrid, E-28040, Madrid, Spain

[§]J. Heyrovský Institute of Physical Chemistry, AS CR, v.v.i., Dolejškova 3, 18223, Prague 8, Czech Republic

[∥]IMDEA-Nanoscience, Campus Universidad Autónoma, 28049-Madrid, Spain

S *Supporting Information*

ABSTRACT: Single molecule charge transport characteristics of buckminsterfullerene-capped symmetric fluorene-based dumbbell-type compound **1** were investigated by scanning tunneling microscopy break junction (STM-BJ), current sensing atomic force microscopy break junction (CS-AFM-BJ), and mechanically controlled break junction (MCBJ) techniques, under ambient conditions. We also show that compound **1** is able to form highly organized defect-free surface adlayers, allowing the molecules on the surface to be addressed specifically. Two distinct single molecule conductance states (called high G_H^1 and low G_L^1) were observed, depending on the pressure exerted by the probe on the junction, thus allowing molecule **1** to function as a mechanically driven molecular switch. These two distinct conductance states were attributed to the electron tunneling through the buckminsterfullerene anchoring group and fully extended molecule **1**, respectively. The assignment of conductance features to these configurations was further confirmed by control experiments with asymmetrically designed buckminsterfullerene derivative **2** as well as pristine buckminsterfullerene **3**, both lacking the G_L feature.
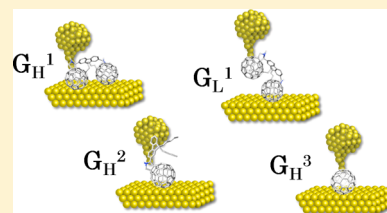
1. INTRODUCTION

Organic molecules employed as active device components within molecular electronic circuits could offer interesting technological opportunities to overcome the scaling limits of silicon-based technology.[1−4] To date, the ease to functionalize allotropes of carbon[5−8] has been exploited in applications in organic photovoltaics[9,10] and, in this context, devices have been prepared, which are capable of reaching energy conversion efficiencies up to 8%.[11] Fullerenes constitute a particular class of molecules that have attracted the attention of the scientific community since their discovery in 1985.[12] They exhibit many unique properties and are particularly important as singular photo- and electroactive species in organic electronics.[13]

In previous years, scanning probe spectroscopy experiments have been carried out on buckminsterfullerene C$_{60}$ adsorbed on noble metal surfaces to address its electronic characteristics.[14−16] These investigations have shown that distinct specific adsorption orientations and geometries as well as intermolecular interactions strongly influence its electronic properties.[17−20] At the same time, advances in the manipulation of single molecules now permit one to contact them between two metal electrodes[21−26] and study their electron transport characteristics to reveal the details of the formed molecular junctions. Thus, the capability of pristine fullerene C$_{60}$ to be

trapped between two electrodes has been envisaged and achieved.[23,27−29] Thanks to its spherical geometry and the multi-interaction configurations of its carbon atoms with metal electrodes, it has been possible to measure the electric conductance across the molecule itself. Additionally, a variety of strategies for the synthesis of molecular wires with two fullerene-type anchoring sites (dumbbell-type molecules) has been developed.[30,31] Such molecules have been designed to act as molecular bridges between two electrodes in break junction studies.[32,33] This new class of molecules is promising due to an ease of functionalization, which allows incorporation of many linkers between the two C$_{60}$ termini.[30,31]

Location of a molecule adsorbed on a surface and determination of its scanning probe spectroscopic properties while maintaining a tunneling gap has been achieved with several molecules, such as naphthalocyanines[34] and redox-active proteins.[35] However, the aim of the current study is to wire a molecule by attaching both of its termini to metal electrodes. These experiments usually require low temperatures and ultrahigh vacuum to suppress mobility of the adsorbed molecules along the substrate.[36] Nonetheless, recent pioneering

studies with dumbbell-type molecules under ambient conditions were reported.[32,33,37] Theoretical calculations have demonstrated that the conductance of these molecules is dominated by the alignment of LUMO orbitals with the electrode Fermi levels.[38] Using a scanning tunneling microscopy (STM) setup, Leary et al.[33] and Gillemot et al.[37] were able to image individual dumbbell molecules attached to gold substrates and recorded subsequently the current through isolated, single molecular nanojunctions by gently touching one of the bulky C_{60} anchoring groups with the STM tip. More than one conductance state was found in these investigations. These experimental findings have been attributed to the existence of distinct metal−molecule−metal geometrical configurations. In this context, our work aims at extending these investigations by exploring electron transport of single molecular dumbbell junctions in a liquid phase with the ultimate goal of potentially exploiting the electroactivity, employing the concept of electrolyte gating (C_{60} is a unique electron acceptor).[39]

In this paper, we report on the transport characteristics of a fluorene-based dumbbell-type molecular wire (molecule **1** in Figure 1), in which two C_{60} moieties are covalently connected
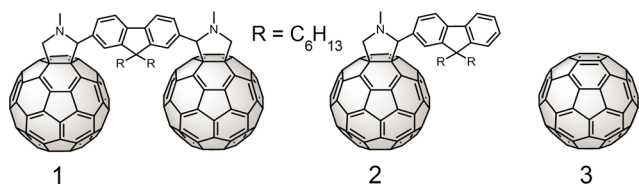

Figure 1. Structures of molecules **1**−**3**.

to a central fluorene unit through the sp^3 carbon atoms of a fused pyrrolidine ring.[40] As this molecule is sufficiently large to be imaged by STM, direct visualization of the molecule prior to the transport measurement allows carrying out single-molecule electrical measurements under well-controlled conditions. Obtained single molecule charge transport characteristics of **1** were compared to those of an asymmetrically designed buckminsterfullerene-capped fluorene-based derivative as well as pristine C_{60} (molecules **2** and **3** in Figure 1). For the first time, we demonstrate STM tip pressure controlled molecular conductance switching (between high and low molecular conductance states), realized under ambient conditions (temperature and pressure) for an isolated molecule **1** at a gold(111)/decane interface.

2. EXPERIMENTAL PROCEDURES

2.1. Synthesis and Characterization of the Compounds. The synthesis of dumbbell-type molecule **1** was carried out by using the well-known Prato reaction on C_{60}.[41,42] Briefly, 2,7-diformyl-9,9-dihexylfluorene reacted with sarcosine (N-methylglycine) in toluene at reflux temperature to form, via a 2-fold 1,3-dipolar cycloaddition reaction of the in situ-generated azomethyne ylide with the double bond of C_{60}, molecule **1**, which was obtained in 10% yield. In turn, 2,7-diformyl-9,9-dihexylfluorene was prepared from commercially available 2,7-dibromofluorene by a dialkylation reaction in position 9, followed by a formylation reaction.[43,44]

To corroborate the expected electronic structure and investigate electron transfer (redox behavior) in molecules **1** to **3**, their solutions were characterized by transmission UV−vis spectroscopy and cyclic voltammetry (see Figures S3 and S4 in Supporting Information (SI) for details).

2.2. STM Imaging Experiments. Bead gold electrodes with 111 facets were used as substrates. They were cleaned by immersion in concentrated sulfuric acid, ensuing electrochemical polishing, and

thorough rinsing with Milli-Q water (Millipore Corp., 18.2 MΩ·cm, 2 ppb TOC). Prior to experiments, they were flame annealed by a butane flame and cooled to room temperature under an argon stream (Carbagas, Alphagaz, 99.999%). The reconstruction of the surface was removed by immersion of the as-prepared electrodes in 0.1 M HCl (diluted from 37%, for analysis, Merck) for 20 min. The electrodes were then thoroughly rinsed with Milli-Q water to remove all chloride anions adsorbed on the electrode surface and dried in a stream of argon. Mechanically cut Pt/Ir wires (80/20, Goodfellow, 0.25 mm in diameter) were employed as STM probes. After assembling an STM Kel-F liquid cell to confine the liquid phase on top of the substrate, 90 μL of decane (99%, Sigma-Aldrich) was added to prevent the adsorption of ambient impurities. The surface was then inspected by STM imaging to verify their absence. Subsequently, 10 μL of 10 μM solution of **1** in toluene (99.8%, Sigma-Aldrich) was added to the liquid phase. In this way, submonolayers of **1** were found to be formed on the Au(111) surface via adsorption from solution. Unlike **1**, molecule **2** was found to be soluble in decane and significantly more soluble in toluene. This allowed carrying out the STM experiments with concentrations of up to 0.1 mM of **2** in decane. For the experiments performed with the molecule **3**, we first immersed the electrode in its 17 μM solution in toluene for 4 min. After rinsing with decane, this modified electrode was mounted to the liquid cell, and subsequently 150 μL of decane was added to protect the surface. In all three cases, the entire STM setup was housed in an all-glass argon-filled environmental chamber.

2.3. Charge Transport Measurements. Charge transport measurements were first performed using the STM-based break junction (STM-BJ) technique.[25,26] The adsorbate-modified substrates were prepared following the protocol described in the Section 2.2. We used electrochemically etched gold wires (Goodfellow, 99.999%, 0.25 mm in diameter) as STM tips to form molecular junctions and investigated their transport characteristics through symmetric Au−molecule (**1**, **2**, or **3**)−Au junctions. The approaching distance between the STM probe and the electrode surface was controlled by a lab-made electronics and dedicated software. Complementary charge transport experiments were carried out with **1** dissolved in mesitylene (98%, Sigma-Aldrich).

Additionally, charge transport experiments with molecule **1** were performed using the mechanically controlled break junction (MCBJ) technique. As this approach relies on the formation of molecular junctions between two horizontally suspended electrodes,[45] we used a modified assembly procedure, which is detailed as follows. First, control transport experiments were carried out in pure decane in the MCBJ liquid cell. The obtained conductance−distance traces showed only quantized gold−gold contact features. Decane was then evaporated by passing an argon flow, and 0.1 mM solution of **1** in toluene (99.8%, Sigma-Aldrich) was then dropcast at 60 °C onto the closed MCBJ nanojunction and dried under an argon flow. This step was repeated four times. Subsequently, the MCBJ nanojunction was opened, and the dropcasting procedure was repeated three more times, employing the same solution of **1** at room temperature. When the solvent was completely evaporated, decane was injected into the liquid cell on top of the central part of the MCBJ liquid cell, to avoid contamination from ambient atmosphere. The system was deoxygenated by purging with an argon stream prior to the conductance measurements.

2.4. Force Measurements. Electromechanical measurements were conducted using the conductive probe atomic force microscopy break junction (CP-AFM) approach.[46,47] Besides monitoring the electric current flowing through the nanojunctions, we simultaneously recorded interaction forces within individual stretching cycles. The experimental setup was based on a modified Agilent Picoplus 5500 system equipped with a 10 μm multimode AFM scanner with a contact-mode nose-cone. The electrically conductive gold-coated Si AFM probes (PPP-NCSTAu, spring constant of 13 N m^{-1}) were purchased from NanoSensors. They were cleaned by immersion in chloroform (98%, Acros Organics) and ethanol (94%, Dr Grogg Chemie AG, Basel) followed by drying in an argon flow (Carbagas, Alphagaz, 99.999%) and subsequent exposure to a UV-ozone cleaner

(Novascan) for 30 min. The parts of the AFM scanner assembly, which were in contact with the solution during the experiments, were rinsed with 2-propanol and afterward dried in an argon flow. The AFM probe was mounted onto the AFM scanner with a metal clamp, which also provided the electrical contact between the conductive gold film on the AFM probe and the lab-built current-to-voltage ($i-V$) converter. Decane and the solution of **1** in toluene were injected to the liquid cell immediately after the mounting of the setup was completed, as described in section 2.2.

2.5. Electrochemical Characterization. The cyclic voltammetric experiments were carried out either with a homemade potentiostat[48] or with commercially available Autolab platform (Metrohm, The Netherlands) in a three-electrode electrochemical cell. All glassware was cleaned by an overnight immersion in caroic acid (see SI for details), followed by repeated boiling, copious rinsing in Milli-Q water, and subsequent drying in an oven. Solutions of molecules **1** to **3** (0.125 mM) were prepared in a mixture of acetonitrile (99.99%, anhydrous, Fisher) and 1,2-dichlorobenzene (99%, anhydrous, Sigma-Aldrich), in a ratio 1:4 v/v. TBAPF$_6$ (99%, Fluka for electrochemistry) was added to all solutions as supporting electrolyte, at a concentration of 0.1 M. The electrode potential scale as well as the electron consumption of **1** to **3** was referenced to the Fc/Fc$^+$ couple (see Figure S4 in SI for details).

3. EXPERIMENTAL RESULTS

The surface adlayers of **1** were first inspected by STM imaging. Figure 2A shows an ordered stripelike arranged monolayer of **1** that coexists with a disordered, mobile phase adsorbed on the unreconstructed Au(111) surface (lower part of the micrograph). Panel B shows a cross-section corresponding to the blue line in Figure 2A.

A periodic adlayer structure was clearly resolved, as observed by the corrugation pattern. The apparent depth of the negative topographic feature (see the dark region in Figure 2A) amounts approximately to
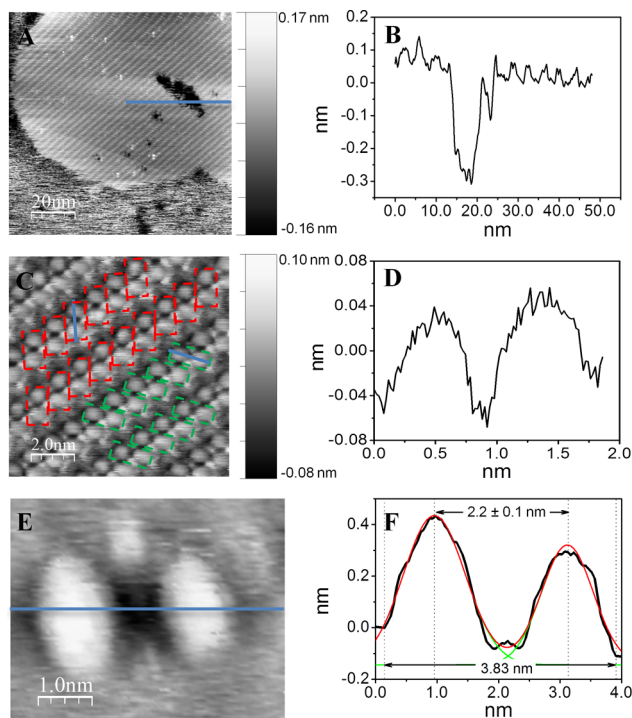
0.35−0.40 nm, which exceeds the monatomic step height of the underlying gold surface (∼0.25 nm) and is assigned to a vacancy within the ordered molecular adlayer. A more resolved picture of the 2D ordered array is achieved by the analysis of the high resolution image displayed in Figure 2C. We observed aligned spherical features that could be attributed to C$_{60}$ anchoring groups within molecules **1**.[49] Furthermore, additional small bright features may be noticed next to the axis defined by two adjacent C$_{60}$ spheres and could be assigned to a highly conductive fluorene linker bridging the two anchoring groups (also see the structure of **1** shown in Figure 1). In Figure 2C, rectangles are meant to denote individual molecules **1** based on two distinct models (red and green) of the surface adlayer. The analysis of profiles pertaining to individual molecules based on these two models revealed a characteristic separation distance between the centers of two adjacent spherical features amounting to (1.00 ± 0.20) nm (Figure 2D).

Since one of our main goals was to address charge transport characteristics of a single dumbbell molecule **1**, we also explored low-coverage adlayer regions. Interestingly, the latter were found to coexist with ordered molecular adlayers and disordered phase, both shown in Figure 2A. In low coverage areas, we identified well-isolated dumbbell molecules. After identifying their location, we monitored them over longer distances and times to explore their strength of attachment to the Au(111) surface. Sufficiently strong binding to the gold substrate is, in this context, essential for locating and lifting of an immobilized single molecule from the substrate to form a molecular bridge between the substrate and the STM tip.[33] Figure 2E shows a single dumbbell molecule **1** adsorbed in the low coverage region. Similarly to what was observed in the monolayer of **1** (Figure 2C), a small bright feature may be noticed next to the axis of the two bright C$_{60}$ spheres, most probably related to the presence of the highly conductive fluorene group bridging the two C$_{60}$ anchoring groups (compare to Figure 1). The cross-section associated with the horizontal blue line in Figure 2E is displayed in Figure 2F. The center-to-center distance between the two C$_{60}$ anchoring sites is estimated as (2.20 ± 0.10) nm. However, it is larger than the theoretically estimated value (1.44 ± 0.04) nm.[50,51] This mismatch may be caused by a thermal- or tip-induced movement of the molecule **1** on the gold surface. On the other hand, the apparent height of the C$_{60}$ anchoring group (0.40 nm, Figure 2F) is in an excellent agreement with literature values (0.35 and 0.40 nm[27] as well as with the vacancy depth in the ordered molecular adlayer (0.35−0.40 nm, Figure 2A,B). The isolated dumbbell molecules could be imaged at very low tunneling set point currents for roughly 1 h provided the entire measurement system was stable enough. However, at higher set point currents, we observed a higher surface mobility caused by displacement of the dumbbell molecule with the STM probe (data not shown). Such mobility reflects limited attractive interactions between the gold surface and the dumbbell molecule. This behavior is different from that in the ordered, closely packed molecular adlayers. In the case of an isolated molecule, there are no attractive intermolecular interactions, which would stabilize the molecule in its fixed position. The observation of the high mobility differs from studies carried out in air with similar dumbbell systems by Leary et al.[33] and Gillemot et al.[37] Therefore, we conclude that the presence of a liquid phase (decane with 10% of toluene added due to solubility reasons) diminishes the strength of attractive interactions of the dumbbell molecules with the gold surface.

Direct visualization of a single molecule prior to charge transport measurements through it is a significant step toward improving the reliability of STM-BJ experiments. Further, working with rather diluted molecular adlayers reduces the risk of their aggregation on the surface and therefore suppresses the interference from intermolecular interactions,[20] leading to preferential formation of metal−single molecule−metal nanojunctions. Additional support for single molecule junctions in the STM-BJ setup is provided by recent concentration-dependent charge transport experiments, which lead to identical conductance, except that the junction formation probability decreases with decreasing concentration.[52]

Upon STM imaging, we proceeded to investigate charge transport characteristics of formed nanojunctions at solid−liquid interfaces. In a

Figure 2. (A) STM image displaying the coexistence of an ordered adlayer of **1** with a mobile phase on an unreconstructed Au(111) surface. Image size 100 × 100 nm^2. (C) 10 × 10 nm^2 high resolution image of the ordered adlayer. (E) 4 × 3 nm^2 image displaying a single molecule **1**. Imaging conditions: $i_{set point}$ = 0.10 nA, V_{bias} = 0.10 V. Apparent height profiles B, D, and F were obtained along the blue lines in A, C, and E, respectively.

first stage, we performed control experiments on the unmodified gold electrodes covered by decane (i.e., without molecules **1**). We recorded hundreds of $G-\Delta z$ traces employing the STM-BJ approach.[25,53] The individual traces were processed further by constructing all-data-point 1D conductance histograms.[52] The latter constructed for gold–gold junctions at a gold/pure decane interface only displayed well-known quantized conductance features at $G \geq G_0$ (data not shown), with $G_0 = 77.5\ \mu S$ being the quantum of conductance. This result confirmed the cleanliness and proper operation of the experimental setup. Next, we introduced a solution of **1** into the liquid cell following the strategy outlined in section 2.2. We then carried out charge transport measurements by recording $G-\Delta z$ characteristics at interfacial regions, where the gold surface was covered by diluted monolayers of **1** (Figure 2E). The low surface coverage of **1** was found to lead to favorable conditions to form single molecule junctions during the continuous approach and retraction probe cycles.

It is known that the transport characteristics through pristine C_{60} in STM-BJ measurements are strongly influenced by the tensile stress and compressive deformation of C_{60} cage generated by the pressure exerted by the tip.[54] To account for this source of conductance variation, we carried out conductance–distance measurements by varying systematically the closest approaching distance of the tip relative to the substrate surface. The latter was achieved by stopping the approach of the probe at a certain position with respect to the surface, as defined by a preset value of the conductance, so-called *trigger conductance* $G_{trigger}$, determined as $G_{trigger} = i_{trigger}/V_{bias}$. The probe vertical movement was controlled via an external feedback loop. The value of $G_{trigger}$ applied in this work spanned the range of $-2.5 \leq \log(G_{trigger}/G_0) \leq 1.5$, where G_0 refers to the conductance quantum. The movement of the probe was either stopped so that a physical contact between the probe and the substrate was prevented ($\log(G_{trigger}/G_0) < 0$), or established ($\log(G_{trigger}/G_0) \geq 0$) (see below).

Figure 3A shows a typical sample $G-\Delta z$ curve acquired with $\log(G_{trigger}/G_0) = -1.0$. The black trace represents the approaching $G-\Delta z$ curve part. The retracting part is plotted as green trace. The majority of the $G-\Delta z$ curves exhibit well-defined plateaus around $\log(G/G_0) \sim -3.0$ to -4.0 and around $\log(G/G_0) \sim -5.0$ to -6.0 that interrupt a characteristic steep decay before and after their appearance, which is assigned to direct electron tunneling through the solvent in the junction both during the approaching and retraction of the STM tip.

Figure 3B and 3C shows further typical withdrawal traces and the corresponding 1D conductance histogram constructed from 558 individual retracting curves, respectively. The histogram displays two well-separated conductance features at high, $\log(G_H^1/G_0) \sim -3.2$, and low, $\log(G_L^1/G_0) \sim -5.9$ region, with both features having a relatively narrow distribution. This observation differs from the results of ref 33, in which the STM-BJ method in air was used and no clearly spaced features were observed using the same representation. We assign the two molecular features to the most probable conductance states, G_H^1 and G_L^1, through a single molecule **1** trapped between metal leads for the particular trigger value $\log(G_{trigger}/G_0) = -1.0$ (justifying thus an increased data density around this value, see Figure 3C). The existence of the two molecular features G_H^1 and G_L^1 is also supported by the two-dimensional representation of the conductance as a function of the tip displacement.[53] Figure 3D shows the 2D conductance histogram, which was constructed with the same data as in panel 3C. The $G-\Delta z$ curves were aligned at $\log(G/G_0) = -6.0$ as a common point (this value is just above the detection limit of the measurement electronics detected when the tip is far from the surface, denoted by asterisks in Figure 3). Panels 3A and 3B (green curves) demonstrate that the high conductance state always precedes the low conductance feature as the tip is being retracted from the adlayer covered substrate (low surface coverage!). On the other hand, the high conductance state follows the occurrence of the low conductance feature for the approaching curves (Figure 3A, black).

We then decreased systematically the distance of the closest approach between the tip and the gold substrate, by increasing the trigger level value. For each $G_{trigger}$ value, we recorded and analyzed the
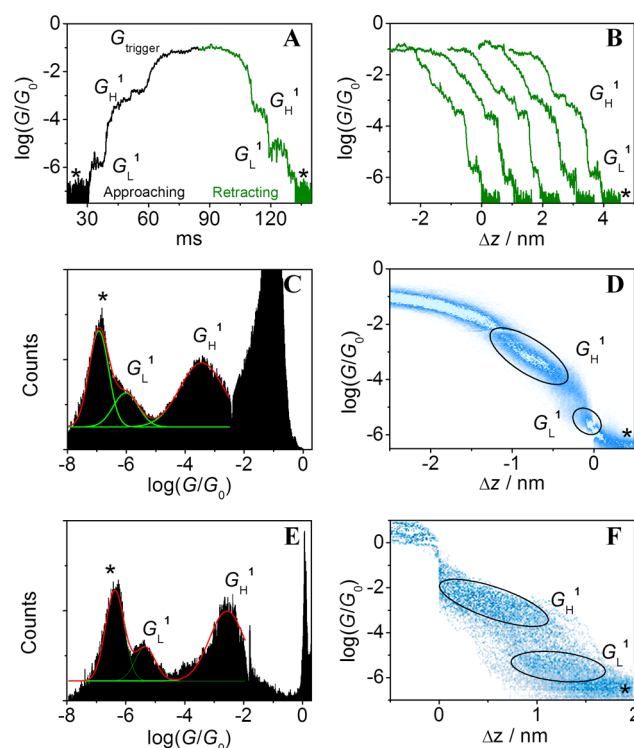

Figure 3. Typical approaching (A, black) and retracting (A, B, green) $G-\Delta z$ curves recorded with $\log(G_{trigger}/G_0) = -1.0$. (C) and (E) show 1D conductance histogram constructed from 558 and 186 withdrawing curves at $\log(G_{trigger}/G_0) = -1.0$ and 1.5, respectively. D and F show 2D histograms corresponding to the data in C and E. The traces were aligned at $\log(G/G_0) = -6.0$ (D) and -0.2 (F). $V_{bias} = 0.03$ V, tip rate $\nu = 58$ nm s^{-1}.

conductance data independently. Figure 3E shows the 1D conductance histogram obtained from 186 withdrawing curves by applying $\log(G_{trigger}/G_0) = 1.5$, i.e., with the physical contact between gold leads created. The sharp peak at $\log(G/G_0) = 0$ represents the conductance of a monatomic gold constriction just before the contact between the two Au electrodes breaks upon further retraction of the tip. The 2D representation of these data displayed in Figure 3F is obtained by aligning all conductance traces at a relative origin of $\log(G/G_0) = -0.2$.[53] This choice is justified by a sharp decay in conductance value upon rupture of the last gold–gold contact in the course of the STM probe retraction.

Figure 4 summarizes the dependence of the molecular conductance on the $G_{trigger}$ value. The existence of both high and low conductance
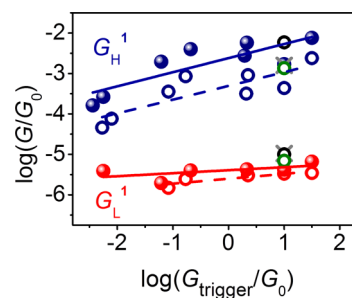

Figure 4. Dependence of the G_H^1 (blue) and G_L^1 (red) values of **1** as a function of $G_{trigger}$. Full and empty circles represent average values obtained from approaching and withdrawing curves, respectively. Gray crosses represent STM-BJ data with **1** dissolved in mesitylene. Black and green empty circles correspond to complementary MCBJ and CP-AFM-BJ data, respectively.

states (G_H^1, G_L^1) is preserved upon varying the $G_{trigger}$ value. We found that G_H^1 increases by up to 2 orders of magnitude as the $G_{trigger}$ value increases (blue circles). However, G_L^1 value remains practically unchanged ($\log(G_L^1/G_0) \sim -5.5$, red circles).

Previous work by Schull et al.[55] in ultrahigh vacuum demonstrated that the conductance of C_{60} rises as the STM tip progressively presses it, because the latter leads to an increase in contact area and an effective decrease of distance between gold leads. We note that the conductance is in all cases larger for the approaching traces (full circles) than for the retracting counterparts (empty circles). We also investigated charge transport properties of **1** dissolved in mesitylene bulk (0.2 mM) to verify whether the molecule **1** could be trapped directly from the solution to form a molecular bridge between the electrodes. Applying $\log(G_{trigger}/G_0) = 1.0$, we obtained the two most probable conductance values $\log(G_H^1/G_0) = -2.8$ and $\log(G_L^1/G_0) = -5.0$, from 2604 withdrawing curves (gray crosses in Figure 4). For details, see Figure S5 in SI.

Complementary conductance measurements using the MCBJ method were carried out to verify the STM-BJ results. Since this technique forms molecular junctions between two horizontally suspended gold electrodes, we employed a different molecular deposition strategy (section 2.3). We recorded 10700 $G-\Delta z$ retracting traces applying $\log(G_{trigger}/G_0) = 1.0$. The conductance distributions obtained upon plotting all retracting traces without any data selection did not show any clear conductance features. Closer inspection of the raw data revealed that no molecular plateaus were observed in most of the cycles. Upon disregarding curves showing only pure tunneling events, i.e., those exhibiting exponential decay upon the tip retraction, we found that only 30% and 7% of the cycles showed the G_H^1 and the G_L^1 states, respectively (see Figure S6 in SI for details). The low junction formation probability is understandable because when employing the MCBJ technique combined with the above-mentioned molecular deposition strategy, one cannot inspect a new surface area as in the STM-BJ technique when the adsorbed molecule is depleted from the studied substrate location. The availability of the molecules bridging the junction is therefore lower and the probability to successfully form molecular junctions is accordingly expected to be decreased. The conductance values extracted from Gaussian fits of the peak-shaped features after the above-mentioned data selection procedure are represented in Figure 4 by black symbols ($\log(G_H^1/G_0) = -2.2$ and $\log(G_L^1/G_0) = -5.0$) (see Figure S6 in SI for details). They are slightly above the trends found by the STM-BJ technique (see dashed lines).

As another complementary experimental technique, we used the conductive-probe atomic force microscopy break junction (CP-AFM-BJ) method.[46,47] The latter provides an access to simultaneous dynamic assessment of the force coupled to the electric current detection during the evolution of the nanojunction.[46,47] This allows finding correlations between molecular conductance and force as the molecular junction breaks. The experimental assembly conditions were the same as for the STM-BJ based charge transport experiment (see section 2.2). We recorded 3769 $G-\Delta z$ retracting curves applying $\log(G_{trigger}/G_0) = 1.0$, while simultaneously monitoring the interaction force between the substrate and the AFM probe. One characteristic retracting conductance−distance trace is shown in Figure 5A. Similarly to STM-BJ, we resolved two most probable conductance features G_H^1 and G_L^1 (highlighted in the 2D conductance histogram shown in Figure 5B by blue ellipses). Additionally, we constructed a master curve (Figure 5B, red profile) by averaging all $\log(G/G_0)$ values (a Gaussian fit used) at all given displacement values Δz. The average molecular conductance values ($\log(G_H^1/G_0) = -2.8 \pm 0.6$ and $\log(G_L^1/G_0) = -5.1 \pm 0.5$) obtained by CP-AFM-BJ technique were extracted from the corresponding 1D histogram (see Figure S7 in SI for details) and are denoted by empty green symbols in Figure 4. The conductance values fit well to the trends found by the STM-BJ technique (dashed lines).

Figure 5C displays the force−distance curve acquired simultaneously with the conductance-distance curve shown in Figure 5A. Three force "jumps" at 0.02, 0.20, and 0.30 nm were observed, i.e., simultaneously with an abrupt decrease of the junction conductance
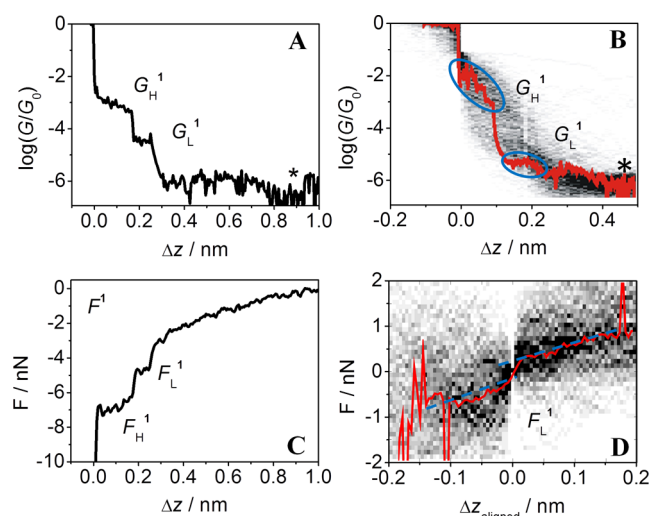

Figure 5. (A) A characteristic withdrawing $G-\Delta z$ curve recorded by CP-AFM-BJ. (B) 2D conductance histogram (black) and corresponding master curve (red). (C) $F-\Delta z$ curve recorded simultaneously with $G-\Delta z$ curve in A. (D) 2D force histogram obtained for F_L^1 feature (black) and corresponding master curve (red). Obtained with $\log(G_{trigger}/G_0) = 1.0$, $V_{bias} = 0.030$ V, $\nu = 50$ nm s^{-1}.

(compare Figure 5C to Figure 5A). The first force jump reflects a plastic deformation of the junction, in the course of which the last Au−Au bond of the junction breaks (the junction conductance drops by 3 orders of magnitude), leaving a molecule **1** bridging the electrodes. The jump at 0.20 nm, denoted as F_H^1 in Figure 5C, reflects a junction transition from the high to the low molecular conductance state, as documented by a concomitant decrease of the junction conductance value from G_H^1 to G_L^1. The latter observed force jump (at 0.30 nm, denoted as F_L^1) originates from the breaking of the molecular junction, as evidenced by an abrupt drop of the conductance value to the detection limit of the measurement electronics ($\log(G/G_0) \approx -6.0$). Similarly, the value of the interaction force gradually reaches 0 nN (Figure, 5C), indicating the departure of the probe from the electrode surface. We constructed a 2D representation of all force−distance traces that showed a clear force jump (F_L^1) at Δz values corresponding to the end of the low conductance feature (G_L^1) by aligning them according to the distance scale shift obtained by the alignment of corresponding conductance−distance traces to $\Delta z_{aligned} = 0$ nm at $G = 0.1$ G_L^1. The resulting force histogram is shown in Figure 5D. The red line superimposed on top of this 2D force histogram displays the force−distance master curve obtained by averaging all force values at each value of the aligned displacement $\Delta z_{aligned}$. The vertical distance of the two force profiles (blue dashed lines in Figure 5D, obtained by linear fitting of the master curve for $\Delta z_{aligned} < 0$ and $\Delta z_{aligned} > 0$, respectively) extrapolated to $\Delta z_{aligned} = 0$, allows estimating the *most probable breaking force* of the junction in the G_L^1 state. This force amounts to ca. 0.4 nN. In a similar way we estimated the rupture force of molecular junctions containing **1** in the G_H^1 state, amounting to ca. 0.7 nN (see Figure S8 in SI for details). Interestingly, the latter force value is very close to the one reported for a (dative covalent) Au−N bond at a gold/molecule interface ($F_{Au-N} = (0.8 \pm 0.2)$ nN[46]). On the other hand, force values obtained in the present work are much smaller than the most probable breaking force value found for the rupture of the Au−Au bond (1.5 nN).[47,56,57] This indirectly indicates that, most probably, an Au−C bond is broken in the junction containing a molecule **1**.

For the data obtained by the STM-BJ technique, we also carried out a careful analysis of the characteristic molecular plateau length (denoted as Δz^{H1} for G_H^1 and Δz^{L1} for G_L^1 features, see Figure 6A,B for characteristic profiles), as a function of the trigger level (Figure 6C,D). The conductance boundaries for the plateau length determination were 0.1 $G_H^1 \leq G \leq 10$ G_H^1 and 0.1 $G_L^1 \leq G \leq 10$
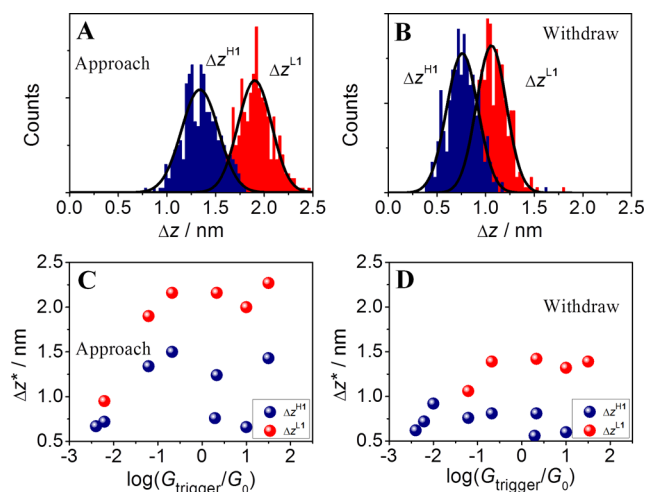
Figure 6. Distributions of Δz_H^1 (blue) and Δz_L^1 (red) obtained from approaching (A) and withdrawing (B) curves using $\log(G_{trigger}/G_0) = -1.2$. (C and D) Dependence of the average plateau length values of approaching (C) and withdrawing (D) events as a function of $G_{trigger}$. $V_{bias} = 0.03$ V, $\nu = 58$ nm s^{-1}.

leads should be remarkably lower than the conductance of a pristine C_{60} due to both the interruption of conjugation by the saturated (sp^3-type) carbon atoms (Figure 1) and the significantly larger length of the fully extended molecule **1**. On the basis of the above arguments, we propose that the two distinct molecular conductance states of **1** (G_H^1 and G_L^1) are originated from two different configurations of the whole molecule of **1** in the junction. They are illustrated in Figure 7. Within
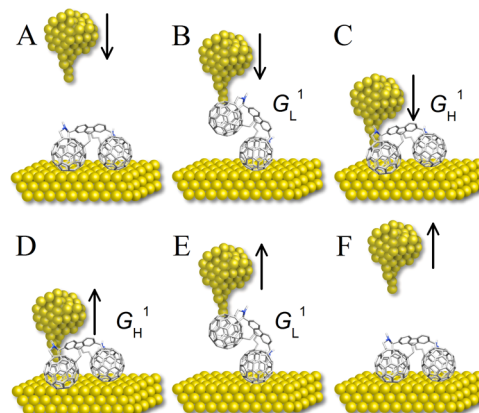

Figure 7. Evolution (approaching/retracting cycles) of the STM-BJ experiment with molecule **1**.

G_L^1 for G_H^1 and G_L^1, respectively. Comparison of Figure 6A and 6B shows that the approaching curves exhibit considerably longer plateau lengths for both conductance states than the withdrawing curves. Additionally, the characteristic plateau length of the G_L^1 state, Δz^{L1}, shows a more noticeable dependence on the $G_{trigger}$ than G_H^1 (Figure 6C,D): Δz^{L1} increases with $G_{trigger}$ (red data points) while the data for Δz^{H1} scatters and does not show a clear trend (blue data points). Finally, Δz^{L1} for the approaching curves reaches a plateau value around 2.0 nm as $\log(G_{trigger}/G_0)$ values are above -1.0 (Figure 6C, red data points). Interestingly, this value is in good agreement with the length of molecule **1** (2.1 ± 0.1 nm)[50] (see below).

The conductance through pristine C_{60} confined between two noble metal leads has been studied in vacuum[15,27,29] and under ambient conditions.[58] More than one conductance state was observed for pristine C_{60} in ultrahigh vacuum experiments. The difference was attributed to the sensitivity of C_{60} to the contact geometry on noble metal electrodes. Berndt et al.[15,55,59,60] showed that different adsorption configurations of C_{60} on metal substrates modify the tunneling current across the molecule when it is contacted by an STM tip. With the exception of ref 27, all observed values are in the range $\log(G/G_0) = -1.0$ to 0.2.[29,37,54,55,58−65] The difference in conductance (up to factor of 20)[55] of these distinct states is, however, much lower than that of the two well-discernible G_H^1 and G_L^1 features that we resolved for **1** (compare blue and red trend lines in Figure 4). We suggest therefore that different contact geometries of the C_{60} anchoring groups cannot account for the existence of these two distinctly observed conductance states of molecule **1**. Additionally, the spread of the most probable conductance values G_H^1 and G_L^1 is comparable to their absolute difference (Figure 3C−F). Molecule **1** possesses a conjugated fluorene system in its central part that leads to efficient delocalization of electric charge between the two C_{60} anchoring groups (Figure 1). However, each C_{60} group is attached to the central fluorene moiety via two electron-saturated linkers. This may, in principle, decrease in a noticeable way the transport efficiency of the whole molecule **1**. The degree of conjugation between the three components (two C_{60} anchoring groups and the linker between them) of related dumbbell-type molecules is crucial for electronic transmission across the molecular bridge.[40] Moreover, the transport through differently capped biphenyls (fluorene including) has been comprehensibly studied[66,67] and could be described by a nonresonant tunneling mechanism. This means that the conductance across the molecular bridge decreases exponentially with its length and is independent of temperature. Therefore, one could then expect that the conductance through an extended molecule **1** connected to two metal

this scenario, the G_L^1 state is assigned to the configuration of molecule **1** bridging the junction, with each C_{60} anchor attached to one of the two metal electrodes, i.e., tip and substrate. The G_H^1 state is attributed to a single C_{60} anchoring group being trapped between the two leads.

The whole stretching cycle may be visualized as follows: In a first stage of the junction evolution, the STM tip is being approached toward the surface modified by molecule **1** (Figure 7A). When the gap separation is close to the molecular length, one C_{60} anchoring group of the molecule jumps into contact with the tip due the thermal motion or applied electric field (Figure 7B). The low conductance state of the junction G_L^1 is reached and the electric current flows through the entire molecule **1**, including the fluorene linker. Alternatively, by the action of the force exerted by the probe on the molecular junction, the molecule **1** may change conformation (not shown in Figure 7B). Due to a short length of the fluorene linker, the two C_{60} moieties may get close to each other, causing their π-systems to overlap and thus creating an additional conductance channel. However, at this stage, we cannot conclusively say if the electron transport in the G_L^1 state of the molecular junction is secured solely by the fluorene linker or is assisted by this additional C_{60}−C_{60} conductance channel. The C_{60} anchoring group attached to the tip is then confined and eventually compressed between tip and substrate (Figure 7C). Alternatively, the sliding of the C_{60} anchoring group along the tip may be possible and the conductance would have contributions from the molecular channel as well as from direct tunneling through the solvent. Upon tip retraction, the decompression or reintroduction of the C_{60} group into the nanogap takes place (Figure 7D). The fully extended molecular junction is formed again via attachment of the molecule between tip and substrate through both C_{60} anchoring groups (Figure 7E). Possibly, an alternative conductance channel leading through two mutually connected C_{60} anchoring groups may be operative (not shown in Figure 7E). Finally, the molecular junction breaks (Figure 7F). This interpretation is supported by the occurrence sequence of the G_H^1 and G_L^1 features (compare Figure 7B to E to Figure 3A) and the evolution of the characteristic plateau length in the two molecular conductance states. As mentioned above, Figure 6 illustrates that the approaching curves exhibit considerably higher plateau lengths for the low conductance feature than the withdrawing curves. The characteristic length of the low conductance state Δz^{L1}, particularly for the approaching curves is rather close to the length of a molecule **1** being completely extended (~2.2 nm). This is reasonable as the molecule jumps into contact with the tip as soon as the latter is close enough to

form an Au–**1**–Au junction, with completely extended molecule **1**. However, the average withdrawing plateau length (Figure 6D) is shorter because during the retraction, the molecule may detach from the tip before complete elongation is reached, due to the weak coupling of C_{60} on Au in decane, caused by the thermal motion of molecule **1** within the junction. On the other hand, the Δz^{H1} values are shorter than the length of a fully extended molecule **1** (Figure 6C,D, blue symbols), and this suggests the trapping of one C_{60} anchoring group, which can be compressed or elongated over much shorter distances than the whole molecule **1**. The characteristic length of the high conductance feature Δz^{H1}, however, is sometimes also larger than the actual size of the C_{60} moiety. This might suggest that the fluorene moiety could attach to the tip which would further stabilize the molecular junctions in the G_L^1 state as it was found in ref 37.

As illustrated in Figure 4, the G_H^1 value increases by up to 2 orders of magnitude as the G_{trigger} value increases (blue data points). By increasing the G_{trigger} value, the effective gap distance between the two electrodes decreases, because the tip exerts a certain pressure on the molecule located within the junction, thus explaining the above trend. The low conductance value G_L^1 is, however, rather insensitive to the G_{trigger} value (red data points in Figure 4). This reflects a certain conformational flexibility of the fully extended molecule **1** in the junction. Recall that the existence of the two conductance states, G_H^1 and G_L^1, was also corroborated by MCBJ and CP-AFM-BJ measurements (see Figures 4 and 5 as well as Figures S6 to S8 in SI).

In an attempt to further rationalize the physical meaning of the two conductance states of **1**, we used the STM-BJ technique to further explore transport characteristics of two additional molecules. Molecule **2** (the asymmetric counterpart of **1**, see Figure 1) bears only one C_{60} anchoring group attached to the fluorene moiety. The second reference molecule to be inspected further was pristine fullerene C_{60} (**3**, see Figure 1). The conductance measurements of **2** were carried out with a rather large bulk concentration in comparison to **1** (0.1 mM for **2** vs 1 μM for **1**), since it was not possible to immobilize molecules **2** on the unreconstructed Au(111) substrate due to their higher solubility in decane.

We explored the molecular conductance and plateau length dependence of **2** and **3** on the G_{trigger} value in the same fashion as for the molecule **1**. The individual G–Δz curves as well as 1D and 2D conductance histograms (Figure 8A,B, data shown for $\log(G_{\text{trigger}}/G_0)$ = 0.40) obtained for **2** displayed only one molecular feature. The dependence of the latter on the G_{trigger} value (Figure 8C) follows

qualitatively well the corresponding dependence constructed for G_H^1 feature (Figure 4, blue circles) and is therefore further referred to as G_H^2.

The corresponding average values of plateau length distributions as a function of the trigger level (Figure 8D) also show that the length over the junction in the G_H^2 state coincides relatively well with that of G_H^1, obtained for the approaching events (Figure 6C). The withdrawing events (Figure 8D, empty circles) obtained for **2** exhibit, however, slightly longer plateaus than in the case of **1** (Figure 6D, blue circles). Additionally, we notice that the highest conductance G_H^2 that we found ($\log(G_H^2/G_0) = -1.01$, Figure 8C) matches the value of ref 37 when only one C_{60} moiety of a related dumbbell compound was trapped between the gold electrodes. The value obtained in this work is also rather close to the results found in the literature for pristine C_{60} immobilized between gold nanoelectrodes in air ($\log(G/G_0) = -1.00$)[58] and vacuum ($\log(G/G_0) = -1.00$ and $\log(G/G_0) = -0.70$)[29,61] but significantly higher than that from another reference[27] ($\log(G/G_0) = -3.60$). Our value is, on the other hand, lower than the conductance of C_{60} trapped between copper ($\log(G/G_0) = -0.87$ to 0.18),[54,55,59,60,62–64] platinum ($\log(G/G_0) = -0.15$),[65] and silver ($\log(G/G_0) = -0.30$)[61] electrodes.

We also carried out transport experiments with molecule **3** and found a unique G_H^3 feature in both the 1D and 2D histograms, as exemplified in Figure 9A,B (the data shown here were obtained with
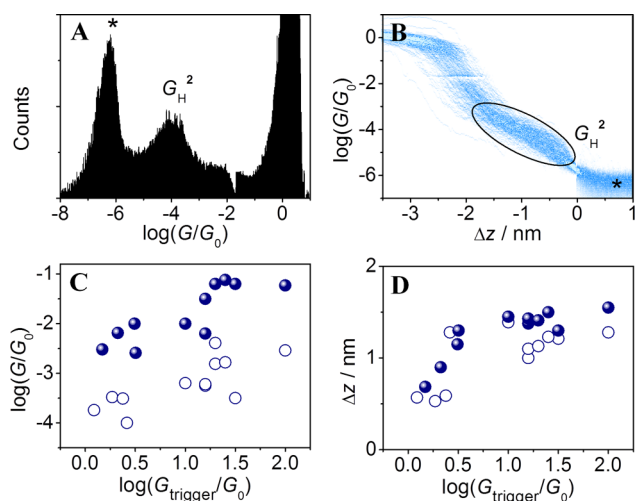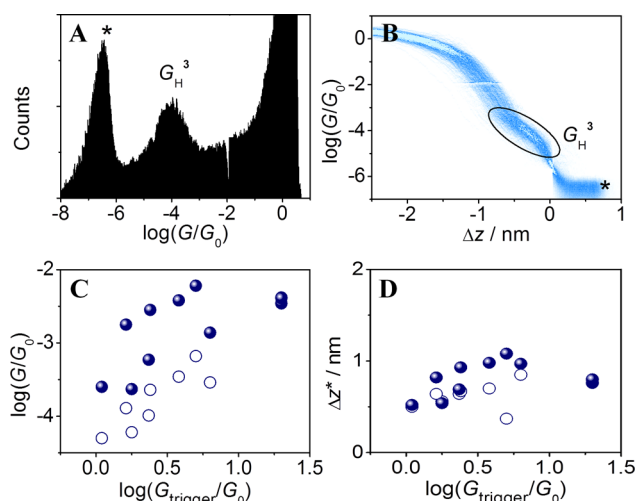
Figure 9. (A) 1D and (B) 2D conductance histograms for **3** constructed from 558 withdrawing curves with $\log(G_{\text{trigger}}/G_0) = 0.40$. (C) Conductance and (D) plateau length dependence on G_{trigger}. V_{bias} = 0.03 V, ν = 58 nm s^{-1}. Filled and empty circles denote the data of the approaching and withdrawing events, respectively.

$\log(G_{\text{trigger}}/G_0) = 0.40$). The G_H^3 dependence on the trigger level (Figure 9C) follows a trend similar to that found for G_H^1 (Figure 4, blue symbols) and G_H^2 (Figure 8C). The maximum conductance found by us for **3** ($\log(G_H^3/G_0) = -2.20$, Figure 9C) is considerably higher than that reported by Joachim et al. ($\log(G/G_0) = -3.6$)[27] but lower than data communicated by the authors of refs 29, 58, and 61 (range of $-1.0 \leq \log(G/G_0) \leq -0.7$). The plateau length dependence on G_{trigger} of **3** is displayed in Figure 9D and indicates that the G_H^3 state remains stable for slightly longer distances as the G_{trigger} value is increased.

Transport experiments with molecules **2** and **3** revealed only one conductance feature (Figures 8A and 9A), which exhibited a dependence of G_H^2 and G_H^3 on G_{trigger} (Figures 8C and 9C) similar to that of G_H^1 (Figure 4, blue circles). The conductance values of all three molecules increase as the trigger level rises. The latter is related to a decreased electrode separation, increasing the transport efficiency and nanogap contact area.

The absolute values of single molecule conductance are however not the same. For example, taking as reference the conductance

Figure 8. (A) 1D and (B) 2D conductance histograms of **2** constructed from 186 withdrawing curves with $\log(G_{\text{trigger}}/G_0)$ = 0.40. (C) Conductance and (D) plateau length dependence on G_{trigger}. V_{bias} = 0.03 V, ν = 58 nm s^{-1}. Filled and empty circles denote the data of approaching and withdrawing events, respectively.

obtained at $\log(G_{trigger}/G_0) = 0.20$, the difference between G_H^2 and G_H^3 amounts to ca. 0.5 order of magnitude (expressed in the logarithmic scale, compare Figures 8C and 9C). Furthermore, the maximum high conductance values of molecules **1** and **3** (both $\log(G_H/G_0) \approx -2.2$, Figures 4 and 9C), are 1 order of magnitude lower than reported values for $C_{60}^{29,37,54,58-65}$ but much larger than the value reported by Joachim et al.[27] The conductance of molecule **2** obtained at $\log(G_{trigger}/G_0) > 1.25$ ($\log(G_H^2/G_0) \approx -1.1$, Figure 8C) is in a good agreement with the former reports.

The difference in conductance observed for G_H^* (* stands for **1**, **2**, or **3**), following the trend $G_H^2 > G_H^1 > G_H^3$, originating from trapping of a C_{60} anchoring group between gold leads, cannot be accounted for by an experimental error. Consideration of the Δz^{H*} values may shed light onto the origin of these differences. As mentioned above, the characteristic length distribution follows the trend $\Delta z^{H2} > \Delta z^{H1} > \Delta z^{H3}$. This suggests that possible attachment of the fluorene bridge in molecules **1** and **2** to the tip may contribute to the longer distances that these molecular structures can be elongated upon existence of the G_H^* feature as compared to molecule **3** (having no fluorene group). Within this scenario, the extra interaction of the fluorene bridge with the gold tip would also involve additional overlapping of the metallic orbitals and the fluorene π-system (see Figure 7). This, in turn, would explain why G_H^1 and G_H^2 are larger than G_H^3 (pristine fullerene does not possess the additional molecular conductance channel).

However, this scenario does not explain why G_H^2 is larger than G_H^1. Our argument to account for this difference is as follows. The presence of an additional free C_{60} anchoring group in **1** (absent in molecule **2**) before formation of the completely elongated molecular junction decreases the stability of the through-fluorene attachment due to steric reasons or thermal movement. In this way, the physical and electronic coupling between fluorene linker in **1** and tip would be less strong, leading to lower transport efficiency (in other words, molecular conductance value) and a correspondingly shorter characteristic plateau length value.

A final comment is related to the possibility of locally addressing energetic states of the molecules **1** to **3** under study. All of them are redox-active, having multiple redox states. Under our experimental electrochemical conditions, neutral and two reduced states of molecules **1** to **3** could be accessible (see Figure S4 in SI for details). Their electroactivity may represent a platform for constructing multistate redox molecular switches, being addressable under electrochemical conditions (i.e., by the electrolyte gating concept). The latter is currently intensively investigated in our laboratory. We also emphasize that the immobilization of the molecules into ordered defect-free adlayers might in the future allow "writing" and "reading" the (electro)chemical state of the molecules, by the aid of a scanning probe, thus allowing the adlayers to serve as molecular memories.

4. CONCLUSIONS

In summary, we have studied charge transport properties of the fluorene-containing dumbbell-type molecular wire **1** under ambient conditions (temperature and pressure) employing the molecular self-assembly deposition strategy in a liquid environment. We were able to image ordered molecular assemblies as well as isolated molecules on the unreconstructed Au(111) substrate. Transport experiments in an STM-BJ configuration revealed two conductance states, G_H^1 and G_L^1 that may be intentionally switched by the pressure exerted by the STM probe. Based on transport studies of related systems performed in ultrahigh vacuum,[59,60] this large difference cannot be accounted for by mere variations in the contact geometry between the C_{60} anchoring groups and the gold leads. The analysis of the evolution of the two states upon approaching and retraction of the STM tip suggests that the G_L^1 feature corresponds to molecular junctions with **1** attached via each C_{60} anchoring site to two distinct leads at opposite sides of the extended molecule. In other words, the molecule is extended

along its axis in the junction. In this state of the molecular junction, the presence of an additional conductance channel may be proposed, running through the two C_{60} anchoring groups, being put together by the pressure exerted by the probe. The G_H^1 feature appears when the distance between the two gold electrodes is significantly shorter. We ascribe this junction configuration to a single C_{60} anchoring group trapped between the two adjacent electrodes. This assignment is also supported by the absence of the G_L^1 states in complementary transport experiments with molecule **2**, which bears only one C_{60} anchoring site and with pristine buckminsterfullerene **3**. The G_H^1 conductance state is strongly dependent on the pressure exerted on the C_{60} group by the tip, with the junction conductance increasing by up to 2 orders of magnitude. The molecular conductance value is the lowest when the C_{60} is touched gently and reaches the maximum when it is strongly compressed or displaced along the edge of the tip. This represents a unique mechanical switching capability of molecule **1**. The agreement in the values of the junction conductance of **1**, **2**, and **3** is rather qualitative. G_H^2 is 1 order of magnitude larger than the corresponding values for G_H^1 and G_H^3.

CP-AFM experiments also allowed exploring the breaking forces of molecular junctions formed by molecule **1** as trapped between two gold leads. We obtained average rupture forces amounting to 0.4 and 0.7 nN for the low and the high molecular conductance state, respectively. The latter value compares well to that obtained in molecular junctions, in which an Au−N bond is broken (0.8 nN). On the other hand, the average values found in this work are markedly lower than that known for the rupture of an Au−Au bond (1.5 nN). This indirectly proves that an Au−C bond is broken in the junction. The unique electrochemical properties of C_{60} and its derivatives provide opportunities to construct multistate redox switching at the single molecule as well as the molecular ensemble level.

■ ASSOCIATED CONTENT

ⓢ Supporting Information
Synthesis and characterization of the compounds **1** to **3**. Additional data of charge transport measurements obtained by MCBJ, CP-AFM-BJ, and STM-BJ. Optimized geometry of **1**. This material is available free of charge via the Internet at http://pubs.acs.org.

■ AUTHOR INFORMATION

Corresponding Authors
*pavel.moreno@dcb.unibe.ch
*alarosa@quim.ucm.es
*viliam.kolivoska@jh-inst.cas.cz
*nazmar@quim.ucm.es

Present Address
†Department of Chemical and Pharmaceutical Sciences, University of Trieste, Piazzale Europa 1, 34127 Trieste, Italy.

Notes
The authors declare no competing financial interest.

■ ACKNOWLEDGMENTS

■ REFERENCES

(1) *Molecular Electronics: An Introduction to Theory and Experiment*; Cuevas, J. C., Scheer, E., Ed.; World Scientific: Singapore, 2010.

(2) Aviram, A.; Ratner, M. A. *Chem. Phys. Lett.* **1974**, *29*, 277−283.

(3) Flood, A. H.; Stoddart, J. F.; Steuerman, D. W.; Heath, J. R. *Science* **2004**, *306*, 2055−2056.

(4) Hush, N. S. An overview of the first half-century of molecular electronics. In *Molecular Electronics III*; Reimers, J. R., Picconatto, C. A., Ellenbogen, J. C., Shashidhar, R., Eds.; New York Acad. Sciences: New York, 2003; Vol. *1006*; pp 01−20.

(5) Guldi, D. M., Martin, N. *Fullerenes: From Synthesis to Optoelectronic Properties*; Academic Publishers: Dordrecht, 2003; Vol. *4*.

(6) Hirsch, A., Brettreich, M. *Fullerenes, Chemistry and Reactions*; Wiley-VCH: Weinheim, 2005.

(7) Langa, F. N., Nierengarten, J.-F. *Fullerenes: Principles and Applications*; RSC: Cambridge, 2007.

(8) Martin, N. *Chem. Commun.* **2006**, 2093−2104.

(9) Thompson, B. C.; Frechet, J. M. J. *Angew. Chem., Int. Ed.* **2008**, *47*, 58−77.

(10) Luis Delgado, J.; Bouit, P.-A.; Filippone, S.; Angeles Herranz, M.; Martin, N. *Chem. Commun.* **2010**, *46*, 4853−4865.

(11) Huo, L.; Zhang, S.; Guo, X.; Xu, F.; Li, Y.; Hou, J. *Angew. Chem., Int. Ed.* **2011**, *50*, 9697−9702.

(12) Kroto, H. W.; Heath, J. R.; Obrien, S. C.; Curl, R. F.; Smalley, R. E. *Nature* **1985**, *318*, 162−163.

(13) Guldi, D. M.; Illescas, B. M.; Atienza, C. M.; Wielopolski, M.; Martin, N. *Chem. Soc. Rev.* **2009**, *38*, 1587−1597.

(14) Lu, X. H.; Grobis, M.; Khoo, K. H.; Louie, S. G.; Crommie, M. F. *Phys. Rev. B* **2004**, *70*, 115418.

(15) Schull, G.; Neel, N.; Becker, M.; Kroeger, J.; Berndt, R. *New J. Phys.* **2008**, *10*, 065012.

(16) Sanchez, L.; Otero, R.; Maria Gallego, J.; Miranda, R.; Martin, N. *Chem. Rev.* **2009**, *109*, 2081−2091.

(17) Grobis, M.; Lu, X.; Crommie, M. F. *Phys. Rev. B* **2002**, *66*, 161408.

(18) Rogero, C.; Pascual, J. I.; Gomez-Herrero, J.; Baro, A. M. *J. Chem. Phys.* **2002**, *116*, 832−836.

(19) Silien, C.; Pradhan, N. A.; Ho, W.; Thiry, P. A. *Phys. Rev. B* **2004**, *69*, 115434.

(20) Torrente, I. F.; Franke, K. J.; Pascual, J. I. *J. Phys.: Condens. Matter* **2008**, *20*, 184001.

(21) Reed, M. A.; Zhou, C.; Muller, C. J.; Burgin, T. P.; Tour, J. M. *Science* **1997**, *278*, 252−254.

(22) Reichert, J.; Ochs, R.; Beckmann, D.; Weber, H. B.; Mayor, M.; Lohneysen, H. V. *Phys. Rev. Lett.* **2002**, *88*, 176804−176804.

(23) Park, H.; Park, J.; Lim, A. K. L.; Anderson, E. H.; Alivisatos, A. P.; McEuen, P. L. *Nature* **2000**, *407*, 57−60.

(24) Cui, X. D.; Primak, A.; Zarate, X.; Tomfohr, J.; Sankey, O. F.; Moore, A. L.; Moore, T. A.; Gust, D.; Harris, G.; Lindsay, S. M. *Science* **2001**, *294*, 571−574.

(25) Xu, B. Q.; Tao, N. J. *Science* **2003**, *301*, 1221−1223.

(26) Li, C.; Pobelov, I.; Wandlowski, T.; Bagrets, A.; Arnold, A.; Evers, F. *J. Am. Chem. Soc.* **2008**, *130*, 318−326.

(27) Joachim, C.; Gimzewski, J. K.; Schlittler, R. R.; Chavy, C. *Phys. Rev. Lett.* **1995**, *74*, 2102−2105.

(28) Parks, J. J.; Champagne, A. R.; Hutchison, G. R.; Flores-Torres, S.; Abruna, H. D.; Ralph, D. C. *Phys. Rev. Lett.* **2007**, *99*, 026601.

(29) Boehler, T.; Edtbauer, A.; Scheer, E. *Phys. Rev. B* **2007**, *76*, 125432.

(30) Segura, J. L.; Martin, N. *Chem. Soc. Rev.* **2000**, *29*, 13−25.

(31) Leary, E.; La Rosa, A.; González, M. T.; Rubio-Bollinger, G.; Agraït, N.; Martín, N. *Chem. Soc. Rev.* **2015**, DOI: 10.1039/C4CS00264D.

(32) Martin, C. A.; Ding, D.; Sorensen, J. K.; Bjornholm, T.; van Ruitenbeek, J. M.; van der Zant, H. S. J. *J. Am. Chem. Soc.* **2008**, *130*, 13198−13199.

(33) Leary, E.; Gonzalez, M. T.; van der Pol, C.; Bryce, M. R.; Filippone, S.; Martin, N.; Rubio-Bollinger, G.; Agrait, N. *Nano Lett.* **2011**, *11*, 2236−2241.

(34) Liljeroth, P.; Repp, J.; Meyer, G. *Science* **2007**, *317*, 1203−1206.

(35) Della Pia, E. A.; Chi, Q.; Jones, D. D.; Macdonald, J. E.; Ulstrup, J.; Elliott, M. *Nano Lett.* **2011**, *11*, 176−182.

(36) Zandvliet, H. J. W. *Chimia* **2012**, *66*, 52−55.

(37) Gillemot, K.; Evangeli, C.; Leary, E.; La Rosa, A.; Teresa Gonzalez, M.; Filippone, S.; Grace, I.; Rubio-Bollinger, G.; Ferrer, J.; Martin, N.; Lambert, C. J.; Agrait, N. *Small* **2013**, *9*, 3812−3822.

(38) Markussen, T.; Settnes, M.; Thygesen, K. S. *J. Chem. Phys.* **2011**, *135*, 144104.

(39) Morita, T.; Lindsay, S. *J. Phys. Chem. B* **2008**, *112*, 10563−10572.

(40) Sorensen, J. K.; Fock, J.; Pedersen, A. H.; Petersen, A. B.; Jennum, K.; Bechgaard, K.; Kilsa, K.; Geskin, V.; Cornil, J.; Bjornholm, T.; Nielsen, M. B. *J. Org. Chem.* **2011**, *76*, 245−263.

(41) Maggini, M.; Scorrano, G.; Prato, M. *J. Am. Chem. Soc.* **1993**, *115*, 9798−9799.

(42) Prato, M.; Maggini, M. *Acc. Chem. Res.* **1998**, *31*, 519−526.

(43) Hughes, G.; Wang, C. S.; Batsanov, A. S.; Fern, M.; Frank, S.; Bryce, M. R.; Perepichka, I. F.; Monkman, A. P.; Lyons, B. P. *Org. Biomol. Chem.* **2003**, *1*, 3069−3077.

(44) Giuseppone, N.; Lehn, J. M. *J. Am. Chem. Soc.* **2004**, *126*, 11448−11449.

(45) Hong, W.; Valkenier, H.; Meszaros, G.; Manrique, D. Z.; Mishchenko, A.; Putz, A.; Garcia, P. M.; Lambert, C. J.; Hummelen, J. C.; Wandlowski, T. *Beilstein J. Nanotechnol.* **2011**, *2*, 699−713.

(46) Xu, B. Q.; Xiao, X. Y.; Tao, N. J. *J. Am. Chem. Soc.* **2003**, *125*, 16164−16165.

(47) Pobelov, I. V.; Meszaros, G.; Yoshida, K.; Mishchenko, A.; Gulcur, M.; Bryce, M. R.; Wandlowski, T. *J. Phys.: Condens. Matter* **2012**, *24*, 164210.

(48) Meszaros, G.; Li, C.; Pobelov, I.; Wandlowski, T. *Nanotechnology* **2007**, *18*, 424004.

(49) Chavy, C.; Joachim, C.; Altibelli, A. *Chem. Phys. Lett.* **1993**, *214*, 569−575.

(50) *CS Chem3D Ultra Molecular Modeling and Analysis*, 7.0.0. ed.; CambridgeSoft, 2001.

(51) Katsonis, N.; Marchenko, A.; Fichou, D. *Synth. Met.* **2003**, *137*, 1453−1455.

(52) Moreno-García, P.; Gulcur, M.; Manrique, D. Z.; Pope, T.; Hong, W.; Kaliginedi, V.; Huang, C.; Batsanov, A. S.; Bryce, M. R.; Lambert, C.; Wandlowski, T. *J. Am. Chem. Soc.* **2013**, *135*, 12228−12240.

(53) Hong, W.; Manrique, D. Z.; Moreno-García, P.; Gulcur, M.; Mishchenko, A.; Lambert, C. J.; Bryce, M. R.; Wandlowski, T. *J. Am. Chem. Soc.* **2012**, *134*, 2292−2304.

(54) Hauptmann, N.; Mohn, F.; Gross, L.; Meyer, G.; Frederiksen, T.; Berndt, R. *New J. Phys.* **2012**, *14*, 073032.

(55) Schull, G.; Frederiksen, T.; Arnau, A.; Sanchez-Portal, D.; Berndt, R. *Nat. Nanotechnol.* **2011**, *6*, 23−27.

(56) Rubio-Bollinger, G.; Bahn, S. R.; Agrait, N.; Jacobsen, K. W.; Vieira, S. *Phys. Rev. Lett.* **2001**, *87*, 026101.

(57) Frei, M.; Aradhya, S. V.; Koentopp, M.; Hybertsen, M. S.; Venkataraman, L. *Nano Lett.* **2011**, *11*, 1518−1523.

(58) Evangeli, C.; Gillemot, K.; Leary, E.; Teresa Gonzalez, M.; Rubio-Bollinger, G.; Lambert, C. J.; Agrait, N. *Nano Lett.* **2013**, *13*, 2141−2145.

(59) Neel, N.; Kroeger, J.; Limot, L.; Frederiksen, T.; Brandbyge, M.; Berndt, R. *Phys. Rev. Lett.* **2007**, *98*, 065502.

(60) Neel, N.; Kroeger, J.; Limot, L.; Berndt, R. *Nano Lett.* **2008**, *8*, 1291−1295.

(61) Zhao, J.; Murakoshi, K.; Yin, X.; Kiguchi, M.; Guo, Y.; Wang, N.; Liang, S.; Liu, H. *J. Phys. Chem. C* **2008**, *112*, 20088−20094.

(62) Schulze, G.; Franke, K. J.; Gagliardi, A.; Romano, G.; Lin, C. S.; Rosa, A. L.; Niehaus, T. A.; Frauenheim, T.; Di Carlo, A.; Pecchia, A.; Pascual, J. I. *Phys. Rev. Lett.* **2008**, *100*, 136801.

(63) Schull, G.; Frederiksen, T.; Brandbyge, M.; Berndt, R. *Phys. Rev. Lett.* **2009**, *103*, 206803.

(64) Strozecka, A.; Muthukumar, K.; Dybek, A.; Dennis, T. J.; Larsson, J. A.; Myslivecek, J.; Voigtlaender, B. *Appl. Phys. Lett.* **2009**, *95*, 133118.

(65) Kiguchi, M. *Appl. Phys. Lett.* **2009**, *95*, 073301.

(66) Venkataraman, L.; Klare, J. E.; Nuckolls, C.; Hybertsen, M. S.; Steigerwald, M. L. *Nature* **2006**, *442*, 904−907.

(67) Mishchenko, A.; Zotti, L. A.; Vonlanthen, D.; Buerkle, M.; Pauly, F.; Carlos Cuevas, J.; Mayor, M.; Wandlowski, T. *J. Am. Chem. Soc.* **2011**, *133*, 184−187.